

Manuscript prepared for Atmos. Meas. Tech.
with version 4.2 of the L^AT_EX class copernicus.cls.
Date: 22 July 2022

Sensitivity of Large-Aperture Scintillometer Measurements of Area-Average Heat Fluxes to Uncertainties in Topographic Heights

Matthew A. Gruber, Gilberto J. Fochesatto

Department of Atmospheric Sciences, College of Natural Science and Mathematics, Geophysical
Institute, University of Alaska Fairbanks, United States of America

Oscar K. Hartogensis

Meteorology and Air Quality Group, Wageningen University, Wageningen, the Netherlands

Correspondence to: Matthew Gruber
(matthewgruber@gi.alaska.edu)

Abstract. Scintillometer measurements allow for estimations of the refractive index structure parameter C_n^2 over large areas in the atmospheric surface layer. Turbulent fluxes of heat and momentum are inferred through coupled sets of equations derived from the Monin-Obukhov similarity hypothesis. One-dimensional sensitivity functions have been produced which relate the sensitivity of heat fluxes to uncertainties in single values of beam height over homogeneous and flat terrain. However, real field sites include variable topography and heterogeneous surfaces. We develop here the first analysis of the sensitivity of scintillometer derived sensible heat fluxes to uncertainties in spacially distributed topographic measurements. For large-aperture scintillometers and independent friction velocity u_* measurements, sensitivity is shown to be concentrated in areas near the center of the beam and where the underlying topography is closest to the beam height. Uncertainty may be greatly reduced by focusing precise topographic measurements in these areas. A new two-dimensional variable terrain sensitivity function is developed for quantitative error analysis. This function is compared with the previous one-dimensional sensitivity function for the same measurement strategy over flat and homogeneous terrain. Additionally, a new method of solution to the set of coupled equations is produced which eliminates computational error. The results are produced using a new methodology for error analysis involving distributed parameters which may be applied in other disciplines.

arXiv:1309.4735v4 [physics.ao-ph] 11 Nov 2013

1 Introduction

Large-aperture scintillometers measure the index of refraction structure parameter C_n^2 over large
 20 areas of terrain in the atmospheric surface layer. The structure parameter for temperature C_T^2 is
 inferred, and this information resolves the sensible heat flux H_S through the application of equations
 derived from the Monin-Obukhov similarity hypothesis (Hartogensis et al., 2003; Moene, 2003).
 The sensible heat flux in the atmospheric surface layer is given by

$$H_S = -\rho c_p u_* T_*, \quad (1)$$

where ρ is the density of air, c_p is the heat capacity at constant pressure, u_* is the friction velocity,
 25 and T_* is the temperature scale (e.g., Monin and Obukhov, 1954; Obukhov, 1971; Sorbjan, 1989;
 Foken, 2006). The temperature scale T_* is resolved by

$$\frac{C_T^2 z^{2/3}}{T_*^2} = \begin{cases} \frac{a}{(1-b\zeta)^{2/3}} & \zeta \leq 0, \\ a(1+c\zeta^{2/3}) & \zeta \geq 0, \end{cases} \quad (2)$$

where z is the height above the ground, $\zeta \equiv z/l$ where l is the Obukhov length (e.g., Sorbjan, 1989),
 and a , b and c are empirical parameters. The values of the empirical parameters are taken to be
 $a = 4.9$, $b = 6.1$, and $c = 2.2$ as seen in Wyngaard et al. (1971) and in Andreas (1989). These values
 30 may not be appropriate for all field sites.

As can be surmised from Eqs. (2) and (3), it is important to know the height z at which C_T^2 is
 being sampled; this corresponds to the scintillometer beam height. The beam height usually varies
 along the beam path. Even if turbulence is being sampled above an extremely flat field, uncertainty
 35 in z will still be present. Previous studies such as Andreas (1989) and Hartogensis et al. (2003) have
 quantified the sensitivity of H_S to uncertainties in z over flat and homogeneous terrain. It is the
 goal of this study to extend the theoretical uncertainty analysis of Andreas (1989) and Hartogensis
 et al. (2003) to take into account variable terrain along the path. The value of this is in the ability
 to evaluate uncertainty estimates for scintillometer measurements over variable terrain, as well as to
 40 study the theoretical effect that the underlying terrain has on this uncertainty.

The studies of Andreas (1989) and of Hartogensis et al. (2003) assume an independently measured
 friction velocity u_* . With large-aperture scintillometers, u_* may be inferred through the Businger-
 Dyer relation of wind stress which is coupled to the Monin-Obukhov equations (e.g., Hartogensis et
 45 al., 2003; Solignac et al., 2009). Alternatively, with displaced-beam scintillometers, path-averaged
 values of the inner-scale length of turbulence l_o can be measured (in addition to C_n^2) which are re-
 lated to the turbulent dissipation rate ϵ , which is in turn related through coupled Monin-Obukhov

equations to u_* (e.g., Andreas, 1992). As a first step towards a variable terrain sensitivity analysis for large-aperture scintillometers, we will assume independent u_* measurements such that the
50 Businger-Dyer equation will not be considered.

In using the Monin-Obukhov similarity hypothesis we are assuming that the flow is stationary and that the terrain is homogeneous. While the topography is not flat, we will assume that it is nearly so and that the surface features are horizontally homogeneous. Heterogeneous terrain implies spacial
55 gradients in fluxes; in this case many authors make the assumption that the scintillometer beam is above the blending height where gradients in fluxes are negligible (e.g., Wieringa, 1986; Mason, 1987; Claussen, 1990, 1995; Meijninger et al., 2002; Hartogensis et al., 2003; Lu et al., 2009). Sensitivity studies have so far been restricted to single values of beam height as in Andreas (1989) and in Appendix A of Hartogensis et al. (2003). Hartogensis et al. (2003) anticipated the quantification
60 of sensitivity in H_S to variable topography for a large-aperture scintillometer strategy with independent u_* measurements.

We are thus considering a large-aperture scintillometer strategy with independent u_* measurements as in Andreas (1989) and in Appendix A of Hartogensis et al. (2003), and we consider the line
65 integral effective beam height formulation from Hartogensis et al. (2003) and Kleissl et al. (2008). The effective height formulation is also discussed in Evans and De Bruin (2011) and in Geli et al. (2012). The assumptions behind this line integral approach are that the profile of C_T^2 above the ground satisfies Eqs. (2) and (3) at any point along the beam path where z is taken to be the local height of the beam above the underlying terrain, and also that H_S is constant vertically and horizontally
70 within the surface layer region sampled by the beam. In this case, two coupled effects must be taken into account. Firstly, the scintillometer is most sensitive to fluctuations in the index of refraction towards the center of its beam. This is due to the optical configuration of the scintillometer system; a unit-less optical path weighting function takes this into account (e.g., Ochs and Wang, 1974; Hartogensis et al., 2003). The second effect is that, in areas where the topography approaches
75 the beam, the C_T^2 being sampled is theoretically more intense than in areas where the terrain dips farther below the beam.

In section 2 of this paper, we define the sensitivity function $S_{H_S,z}(u)$ for the sensible heat flux H_S as a function of variable topography $z(u)$, where u is the normalized distance along the beam path.
80 In section 3, we solve for $S_{H_S,z}(u)$ for any general given $z(u)$. In section 4 we visualize the results by applying the resulting sensitivity function to the topography of a real field site in the North Slope of Alaska. We then apply the resulting sensitivity function to examples of synthetic beam paths. In section 5 we discuss our results, and we conclude in section 6.

2 Definition of the Sensitivity Function $S_{H_S, z}(u)$

85 Under stable conditions ($\zeta > 0$), the set of equations to consider consists of Eqs. (1) and (2), as well as

$$\zeta = \frac{\kappa g T_* z_{eff}}{u_*^2 T}, \quad (4)$$

$$\frac{C_T^2 z_{eff}^{2/3}}{T_*^2} = a(1 + c\zeta^{2/3}) \rightarrow (\pm)T_* = \sqrt{\frac{C_T^2}{a}} \frac{z_{eff}^{1/3}}{(1 + c\zeta^{2/3})^{1/2}}, \quad (5)$$

$$z_{eff} = \left(\int_0^1 z(u)^{-2/3} G(u) du \right)^{-3/2}, \quad (6)$$

90 where z_{eff} is the effective beam height derived in Kleissl et al. (2008) based on the theory from Hartogensis et al. (2003), $z(u)$ is the height of the beam along the normalized path length u , $G(u)$ is the optical path weighting function, g is gravitational acceleration, and κ is the von Kármán constant.

For unstable conditions ($\zeta < 0$) Eqs. (1), (3) and (4) are still considered, but Eqs. (5) and (6) are
95 replaced by

$$\frac{C_T^2 z_{eff}^{2/3}}{T_*^2} = \frac{a}{(1 - b\zeta)^{2/3}} \rightarrow (\pm)T_* = \sqrt{\frac{C_T^2}{a}} z_{eff}^{1/3} (1 - b\zeta)^{1/3}, \quad (7)$$

$$z_{eff} = \frac{z_{eff}}{2b\zeta} \left(1 - \sqrt{1 - \frac{4b\zeta}{z_{eff}} \left[\int_0^1 z(u)^{-2/3} \left(1 - b\zeta \frac{z(u)}{z_{eff}} \right)^{-2/3} G(u) du \right]^{-3/2}} \right), \quad (8)$$

where z_{eff} is derived in Hartogensis et al. (2003).

100 The propagation of uncertainty from source measurements such as $z(u)$ to derived variables such as H_S will be evaluated in the context of the inherent assumptions behind the theoretical equations. A good estimate of the uncertainty in the derived variables that results from small errors in source measurements is given by

$$\sigma_f = \sum_{i=1}^N \left(\frac{\partial f}{\partial x_i} \right) \sigma_{x_{s_i}} + \sqrt{\sum_{i=1}^N \left(\frac{\partial f}{\partial x_i} \right)^2 \sigma_{x_{r_i}}^2} + \sigma_{f_c}, \quad (9)$$

where derived variable f is a function of source measurement variables x_1, x_2, \dots, x_N with respective
105 systematic error $\sigma_{x_{s_1}}, \sigma_{x_{s_2}}, \dots, \sigma_{x_{s_N}}$ and with respective independent Gaussian distributed uncertainties with standard deviations $\sigma_{x_{r_1}}, \sigma_{x_{r_2}}, \dots, \sigma_{x_{r_N}}$ as seen in Taylor (1997). The numerical indices indicate different independent variables, such as T , P , or z , for example. Computational error on f due to the inaccurate solution of the theoretical equations is represented by σ_{f_c} . The first and last terms in Eq. (9) represent an offset from the true solution (inaccuracy), whereas the central square

110 root term represents the breadth of uncertainty due to random error (imprecision). The source measurement variables being considered here are P , T , C_n^2 , λ , $z(u)$, and u_* .

It is convenient to re-write Eq. 9 as

$$\frac{\sigma_f}{f} = \sum_{i=1}^N \left(S_{f,x} \frac{\sigma_{x_{s_i}}}{x_{s_i}} \right) + \sqrt{\sum_{i=1}^N \left(S_{f,x}^2 \frac{\sigma_{x_{r_i}}^2}{x_{r_i}^2} \right)} + \frac{\sigma_{f_c}}{f}, \quad (10)$$

where the sensitivity functions $S_{f,x}$ are defined as

$$S_{f,x} \equiv \frac{x}{f} \left(\frac{\partial f}{\partial x} \right). \quad (11)$$

115 Sensitivity functions such as these are developed in Andreas (1989) and Andreas (1992). They are each a measure of the portion of relative error in a derived variable f resulting from relative error on the individual source measurement variable x . The problem of resolving the uncertainty on the derived variables is a matter of identifying the magnitude and character of the source measurement uncertainties, and then solving for the partial derivative terms in Eqs. (9) and (11).

120

We seek a solution to the sensitivity function of sensible heat flux as a function of topography $S_{H_S,z}$. The sensitivity function $S_{H_S,z}$ is a function only of ζ in the flat and homogeneous terrain case as seen in Andreas (1989). We may imagine that since $z(u)$ is distributed over one dimension instead of a single value of z , $S_{H_S,z}$ will be a function of both ζ and u . We are thus aiming to expand S_z seen in Fig. (4) of Andreas (1989) from one dimension to two. This extra dimension will come from the fact that some derived variables such as z_{eff} are functions of an integral over continuous variables $z(u)$ and $G(u)$, where we consider for generality that $z(u)$ has a continuous uncertainty $\sigma_z(u)$. To illustrate this we re-write for example Eq. (6) as

125

$$z_{eff} = \left(\int_0^1 z(u)^{-2/3} G(u) du \right)^{-3/2} = \left(\lim_{N \rightarrow \infty} \sum_{i=1}^N z_i^{-2/3} G_i \cdot (1/N) \right)^{-3/2}, \quad (12)$$

130 where subscript i indicates that $u = (i/N)$. The propagation of error defined by Eq. 9 involves derivatives of the dependent variables as functions of all the independent variables, where each z_i is independent. For such a partial derivative term we have

$$\begin{aligned}
\left(\frac{\partial z_{eff}}{\partial z_k}\right) &= -\frac{3}{2} \left(\lim_{N \rightarrow \infty} \sum_{i=1}^N z_i^{-2/3} G_i \cdot (1/N) \right)^{-5/2} \frac{\partial}{\partial z_k} \left(\lim_{N \rightarrow \infty} \sum_{i=1}^N z_i^{-2/3} G_i \cdot (1/N) \right), \\
&= -\frac{3}{2} \left(\lim_{N \rightarrow \infty} \sum_{i=1}^N z_i^{-2/3} G_i \cdot (1/N) \right)^{-5/2} \frac{\partial}{\partial z_k} \left(\lim_{N \rightarrow \infty} \sum_{i=1}^N z_i^{-2/3} G_i \cdot (1/N) \delta_{ik} \right), \\
135 \quad &= -\frac{3}{2} \left(\lim_{N \rightarrow \infty} \sum_{i=1}^N z_i^{-2/3} G_i \cdot (1/N) \right)^{-5/2} \frac{\partial}{\partial z_k} z_k^{-2/3} G_k \cdot (1/N), \\
&= \left(\lim_{N \rightarrow \infty} \sum_{i=1}^N z_i^{-2/3} G_i \cdot (1/N) \right)^{-5/2} z_k^{-5/3} G_k \cdot (1/N). \tag{13}
\end{aligned}$$

This anticipates the definition of a new differential operator which is the same as a normal partial derivative in all steps including chain rule, product rule, etc., except upon the application of the Leibniz rule while differentiating the primary variable, whereupon we multiply the integrand by a Dirac-Delta function. We can name this operator the ‘‘Dirac-Leibniz’’ derivative, and we denote it here as $\frac{\delta}{\delta x}$ (as opposed to $\frac{\partial}{\partial x}$) when differentiating with respect to x . Using continuous notation and again differentiating Eq. 12, we can write

$$\begin{aligned}
\left(\frac{\delta z_{eff}}{\delta z}(u)\right) &= \frac{\delta}{\delta z} \left(\int_0^1 z(u)^{-2/3} G(u) du \right)^{-3/2}, \\
&= -\frac{3}{2} \left(\int_0^1 z(u)^{-2/3} G(u) du \right)^{-5/2} \frac{\delta}{\delta z} \left(\int_0^1 z(u)^{-2/3} G(u) du \right), \\
145 \quad &= -\frac{3}{2} \left(\int_0^1 z(u)^{-2/3} G(u) du \right)^{-5/2} \frac{\partial}{\partial z} \left(\int_0^1 z(U)^{-2/3} G(U) \delta(U-u) dU \right), \\
&= \left(\int_0^1 z(u)^{-2/3} G(u) du \right)^{-5/2} z(u)^{-5/3} G(u). \tag{14}
\end{aligned}$$

Note that $\frac{\partial z_{eff}}{\partial z_k} = \frac{1}{N} \left(\frac{\delta z_{eff}}{\delta z} \right)_k$; it can also be derived that $\frac{\partial H_S}{\partial z_k} = \frac{1}{N} \left(\frac{\delta H_S}{\delta z} \right)_k$.

We thus define

$$S_{H_S, z}(u) \equiv \frac{z(u)}{H_S} \left(\frac{\delta H_S}{\delta z}(u) \right), \tag{15}$$

150 as the sensitivity function of sensible heat flux H_S to uncertainties in variable topography $z(u)$. It is our goal to evaluate equation 15.

3 Solution of the Sensitivity Function $S_{H_S, z}(u)$

3.1 Stable Conditions ($\zeta > 0$)

Under stable conditions the set of Eqs. (1, 2, 4, 5, 6) is coupled in l through ζ ; we begin de-coupling
 155 them by combining Eqs. (4) and (5) to obtain

$$\zeta = (\pm) \frac{\kappa g z_{eff}^{4/3} \sqrt{C_T^2}}{u_*^2 T \sqrt{a(1+c\zeta^{2/3})^{1/2}}}. \quad (16)$$

Since $\zeta > 0$, the unsolved sign is positive. With the substitution

$$\hat{\Lambda} \equiv \frac{\kappa^2 g^2 C_T^2}{u_*^4 T^2 a}, \quad (17)$$

we re-arrange Eq. (16) to obtain

$$\zeta^2 + c\zeta^{8/3} - \hat{\Lambda} z_{eff}^{8/3} = 0, \quad (18)$$

where z_{eff} in the stable case is determined by a-priori known functions $z(u)$ and $G(u)$ through
 Eq. (6). The value of $\hat{\Lambda}$, including C_T^2 , is directly determined from the source measurements. The
 160 solution of Eq. (18) follows by re-writing it as a fourth order algebraic equation in $\zeta^{2/3}$:

$$(\zeta^{2/3})^3 + c(\zeta^{2/3})^4 - \hat{\Lambda} z_{eff}^{8/3} = 0, \quad (19)$$

or more practically, it can be solved through fixed point recursion on the function

$$\zeta = \sqrt{\frac{\hat{\Lambda} z_{eff}^{8/3}}{1+c\zeta^{2/3}}} \equiv \hat{F}(\zeta), \quad (20)$$

where we must consider the positive root. Note that since Eq. (19) is below fifth order, Galois theory
 states that it has an explicit solution form (e.g., Edwards, 1984). It is thus possible in theory to write
 $H_S = h(z(u), C_n^2, P, T, \lambda, u_*)$ where h is an explicit function of the source measurements, however
 165 it would be quite an unwieldy equation.

We do not need an explicit solution in order to study the sensitivity; we can use the chain rule
 and implicit differentiation as in Gruber and Fochesatto (2013). We establish the variable inter-
 dependency using Eq. (18) as a starting point. The tree diagram for any set of source measurements
 170 in stable conditions is seen in Fig. (1). The source measurements are at the ends of each branch, and
 all other variables are dependent.

The required global partial derivatives are now defined through the variable definitions, the above
 equations, and the tree diagram. For example, we have

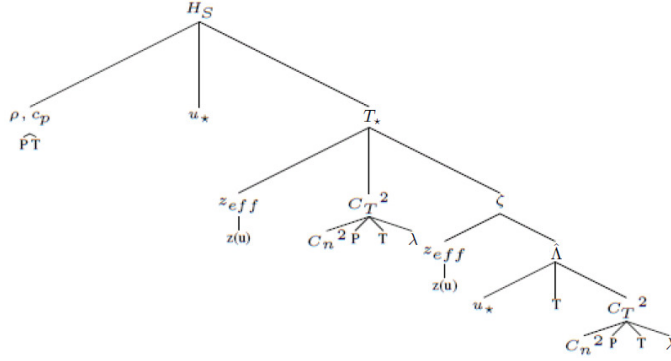


Fig. 1. Variable inter-dependency tree diagram for the stable case ($\zeta > 0$). The source measurement variables are at the end of each branch; all other variables are derived.

$$\left(\frac{\delta H_S}{\delta z}(u)\right) = \left(\frac{\partial H_S}{\partial T_*}\right) \left(\left(\frac{\partial T_*}{\partial z_{eff}}\right)_\zeta + \left(\frac{\partial T_*}{\partial \zeta}\right)_{z_{eff}} \left(\frac{\partial \zeta}{\partial z_{eff}}\right) \right) \left(\frac{\delta z_{eff}}{\delta z}(u)\right). \quad (21)$$

175 We'll need some derivatives which we are not able to directly retrieve from explicit definitions. By implicitly differentiating Eq. (18) under the guidance of the tree diagram seen in Fig. (1), we derive

$$\left(\frac{\partial \zeta}{\partial z_{eff}}\right) = \left(\frac{4\hat{\Lambda}z_{eff}^{5/3}}{3\zeta + 4c\zeta^{5/3}}\right) = \frac{1}{z_{eff}} \left(\frac{4\zeta(1+c\zeta^{2/3})}{3+4c\zeta^{2/3}}\right). \quad (22)$$

The Dirac-Leibniz derivative term $\left(\frac{\delta z_{eff}}{\delta z}(u)\right)$ for stable conditions has been evaluated in Eq. 180 (14).

3.2 Unstable Conditions ($\zeta < 0$)

Under unstable conditions the set of Eqs. (1, 3, 4, 7, 8) is coupled in l through ζ ; note that z_{eff} is coupled to ζ in the unstable case. We combine Eqs. (4) and (7) to obtain

$$\zeta = (\pm) \frac{\kappa g \sqrt{C_T^2}}{u_*^2 T \sqrt{a}} z_{eff}^{4/3} (1 - b\zeta)^{1/3}. \quad (23)$$

Since $\zeta < 0$, the sign is negative. With the substitution $\check{\Lambda} \equiv \left(\frac{\kappa g \sqrt{C_T^2}}{u_*^2 T \sqrt{a}}\right)^{3/4}$, this leads to

$$z_{eff} = \frac{1}{\check{\Lambda}} \frac{(-\zeta)^{3/4}}{(1 - b\zeta)^{1/4}} \rightarrow \frac{\zeta}{z_{eff}} = -\check{\Lambda} (b\zeta^2 - \zeta)^{1/4}. \quad (24)$$

185 We substitute Eq. (24) into Eq. (8) to obtain

$$\zeta = \frac{1}{2b} \left(1 - \sqrt{1 + 4b\check{\Lambda}(b\zeta^2 - \zeta)^{1/4} \left[\int_0^1 (z(u) + bz(u)^2 \check{\Lambda}(b\zeta^2 - \zeta)^{1/4})^{-2/3} G(u) du \right]^{-3/2}} \right) \equiv \check{F}(\zeta). \quad (25)$$

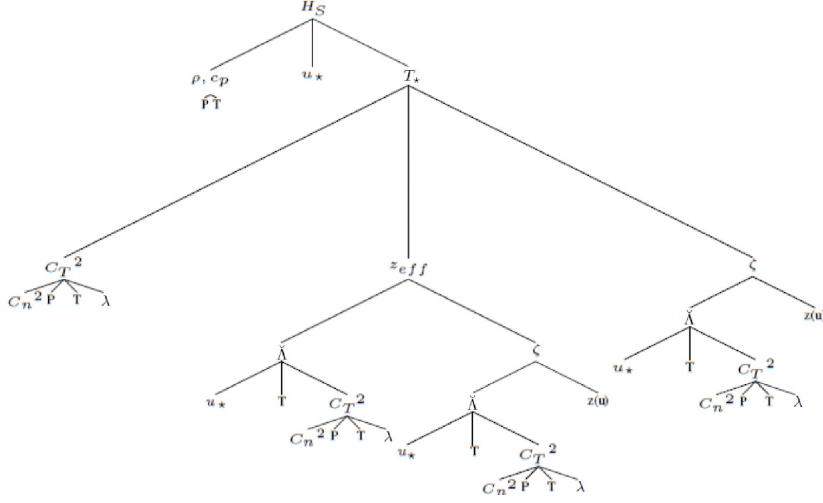


Fig. 2. Variable inter-dependency tree diagram for the unstable case ($\zeta < 0$). The source measurement variables are at the end of each branch; all other variables are derived.

This single equation is in the single unknown ζ since $z(u)$, $G(u)$ and $\check{\Lambda}$ are known; it is also in the fixed point form $\zeta = \check{F}(\zeta)$. The tree diagram for the unstable case is seen in Fig. (2). Evaluation of global partial derivatives proceeds analogously to the stable case as in Eq. (21). Now we have

$$\left(\frac{\delta H_S}{\delta z}(u) \right) = \left(\frac{\partial H_S}{\partial T_*} \right) \left(\left(\frac{\partial T_*}{\partial z_{eff}} \right) \left(\frac{\partial z_{eff}}{\partial \zeta} \right) + \left(\frac{\partial T_*}{\partial \zeta} \right)_{z_{eff}} \right) \left(\frac{\delta \zeta}{\delta z}(u) \right). \quad (26)$$

190 To pursue the solution of $S_{H_S, z}(u)$, we will need to solve for $\left(\frac{\partial z_{eff}}{\partial \zeta} \right)$ by the differentiation of Eq. (24):

$$\left(\frac{\partial z_{eff}}{\partial \zeta} \right) = \frac{(2b\zeta - 3)}{4\check{\Lambda}(-\zeta)^{1/4}(1-b\zeta)^{5/4}} = \frac{z_{eff}(3-2b\zeta)}{4\zeta(1-b\zeta)}. \quad (27)$$

We can solve for $\left(\frac{\delta \zeta}{\delta z}(u) \right)$ by implicit differentiation of Eq. (25). In finding $\left(\frac{\delta \zeta}{\delta z}(u) \right)$, it is useful to define

$$f(\check{\Lambda}, \zeta(z(u), \check{\Lambda}), z(u)) \equiv 1 + 4b\check{\Lambda}(b\zeta^2 - \zeta)^{1/4} \left[\int_0^1 (z(u) + bz(u)^2 \check{\Lambda}(b\zeta^2 - \zeta)^{1/4})^{-2/3} G(u) du \right]^{-3/2}, \quad (28)$$

195 where, from Eqs. (25) and (28), we have

$$\sqrt{f} = (1 - 2b\zeta). \quad (29)$$

From Eq. (28), we have that

$$\left(\frac{\delta f}{\delta z}(u)\right) = \left(\frac{\partial f}{\partial \zeta}\right) \left(\frac{\delta \zeta}{\delta z}(u)\right) + \left(\frac{\delta f}{\delta z}(u)\right)_{\zeta}, \quad (30)$$

such that, from Eqs. (25), (28), and (29), we derive

$$\left(\frac{\delta \zeta}{\delta z}(u)\right) = \frac{-\left(\frac{\delta f}{\delta z}(u)\right)_{\zeta}}{\left(\frac{\partial f}{\partial \zeta}\right) + 4b(1-2b\zeta)}, \quad (31)$$

$$= \frac{-\frac{4\zeta(1-b\zeta)}{(1-2b\zeta)}(z(u) + bz(u)^2\lambda(b\zeta^2 - \zeta)^{\frac{1}{4}})^{-\frac{5}{3}}(1+2bz(u)\lambda(b\zeta^2 - \zeta)^{\frac{1}{4}})G(u)}{\left[\int_0^1 (z(u) + bz(u)^2\lambda(b\zeta^2 - \zeta)^{\frac{1}{4}})^{-\frac{2}{3}}G(u)du\right] + b\lambda(b\zeta^2 - \zeta)^{\frac{1}{4}}\left[\int_0^1 (z(u) + bz(u)^2\lambda(b\zeta^2 - \zeta)^{\frac{1}{4}})^{-\frac{5}{3}}z(u)^2G(u)du\right] - \frac{4(b\zeta^2 - \zeta)^{\frac{3}{4}}}{\lambda}\left[\int_0^1 (z(u) + bz(u)^2\lambda(b\zeta^2 - \zeta)^{\frac{1}{4}})^{-\frac{2}{3}}G(u)du\right]^{\frac{5}{2}}}. \quad (32)$$

200 All the information we need to solve for $S_{H_{S,z}}(u)$ is now resolved.

3.3 Full Expression for the Sensitivity Function $S_{H_{S,z}}(u)$

Since we are considering an independent u_* measurement, we have that $S_{T_*,z}(u) = S_{H_{S,z}}(u) = \frac{z(u)}{T_*} \left(\frac{\delta T_*}{\delta z}(u)\right)$. We obtain

$$S_{T_*,z}(u) = \begin{cases} \frac{z(u)^{-2/3}G(u)}{\int_0^1 z(u)^{-2/3}G(u)du} \left(\frac{1}{3+4c^2/3}\right) & \zeta > 0, \quad (33) \\ -z(u)(z(u) + bz(u)^2\lambda(b\zeta^2 - \zeta)^{\frac{1}{4}})^{-\frac{5}{3}}(1+2bz(u)\lambda(b\zeta^2 - \zeta)^{\frac{1}{4}})G(u) & \zeta < 0, \quad (34) \end{cases}$$

where the individual terms of $\left(\frac{\delta T_*}{\delta z}(u)\right)$ are given in Appendices (7) and (8).

4.1 Imnavait Creek Basin Field Campaign

As an example we use topographic data from the Imnavait Creek Basin field site where there is a campaign to determine large-scale turbulent fluxes in the Alaskan tundra; it is seen in Figs. (3(a)) and (4). We assume for simplicity that vegetation patterns, water availability, and other changes across the basin which could affect the flow in the atmospheric surface layer do not represent a significant source of surface heterogeneity. The elevation data seen in Fig. (3(a)) is from a 5 m resolution Digital Elevation Map (DEM) which has a roughly 0.5 m standard deviation in a histogram of the difference between the DEM elevations and 50 randomly distributed GPS ground truth points, as seen in Fig. (3(b)). Note that the systematic offset between the DEM and the GPS ground truth measurements does not contribute to systematic error in $z(u)$. Note also that some of this spread in data may be due to an active permafrost layer.

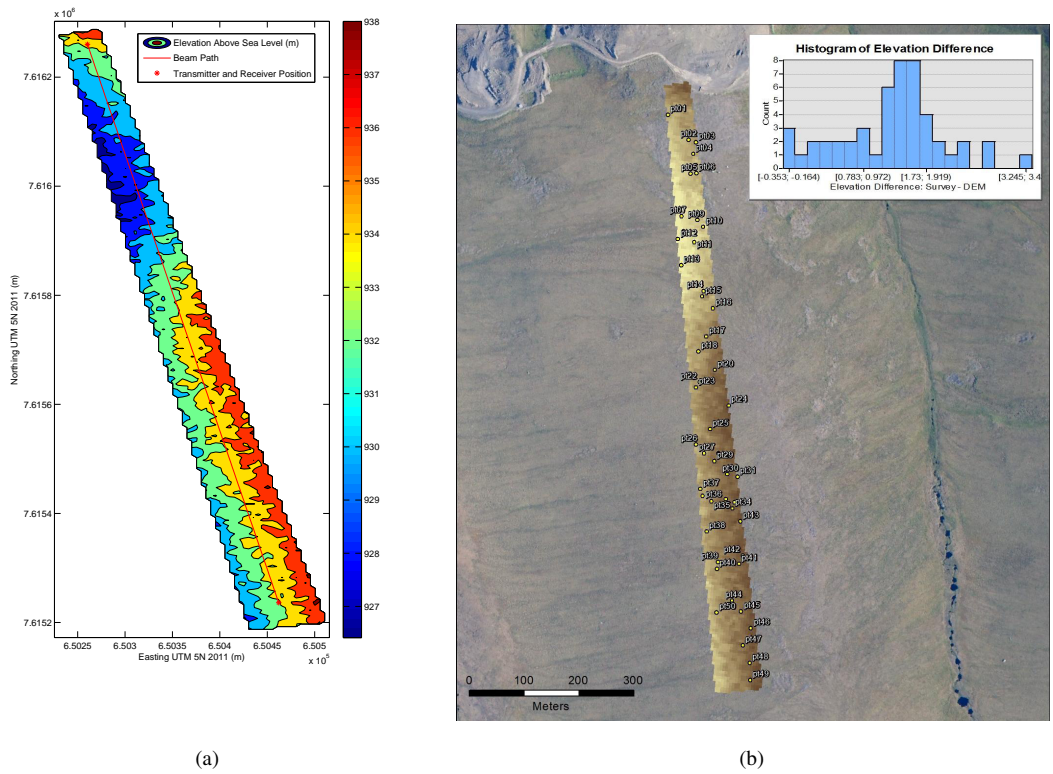


Fig. 3. Topography and space view of Imnavait Creek Basin, North Slope of Alaska. The scintillometer beam runs roughly North-South on a 1.04 km path. The emitter and receiver are each raised off the ground by 3.8 m. Vegetation along the path is representative of Arctic tundra. Superimposed is a histogram of 50 points of GPS ground truth elevation minus DEM elevation.

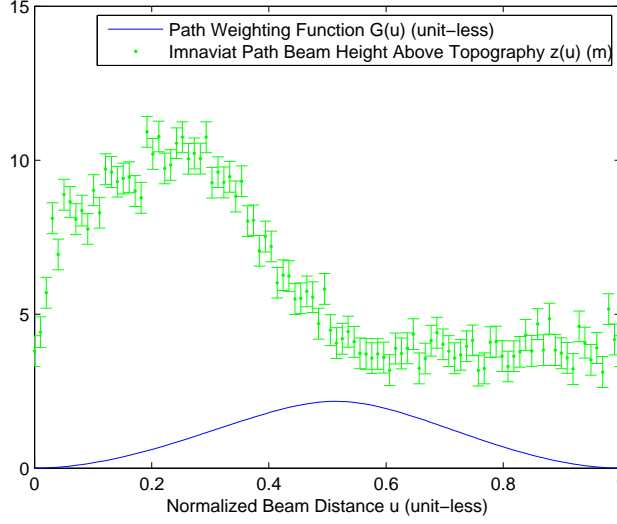


Fig. 4. Height of the beam above the ground z and the path weighting function G as functions of normalized beam distance u , using the Imnavait experimental site as seen in Fig. (3(a)). Uncertainties are based on the approximate standard deviation in the histogram in Fig. (3(b)), although they don't influence the analysis presented in this study.

For this field site, we can solve for ζ in unstable conditions through Eq. 25. As can be seen in Fig. (5), we arrive at the solution for ζ with the recursively defined series $[\check{F}(\zeta_{guess}), \check{F}(\check{F}(\zeta_{guess})), \check{F}(\check{F}(\check{F}(\zeta_{guess}))), \dots]$ which is guaranteed to converge monotonically for any $\zeta_{guess} < 0$. A plot of ζ as a function of $\check{\Lambda}$ for 220 this field site is seen in Fig. (6). Note that the relationship between ζ and $\check{\Lambda}$ is bijective; any value of $\check{\Lambda}$ is uniquely associated with a value of ζ for $\zeta < 0$.

Considering the field case study of the Imnavait Creek Basin where the height of the beam over the terrain $z(u)$ and the standard path weighting function $G(u)$ are seen in Figs. (3(a)) and (4), Eqs. 225 (33) and (34) lead to the sensitivity function seen in Fig. (7). Note that $S_{H_S, z}(u)$ is a function of only u and ζ , since, for any one beam height transect $z(u)$, $\check{\Lambda}$ is mapped bijectively with respect to ζ through Eq. (25), as seen in Fig. (6).

Note that if we consider a constant ratio of $\frac{\sigma_z(u)}{z(u)}$, the term in, for example Eq. (10), can be 230 re-written as

$$\int_0^1 \frac{\sigma_z(u)}{z(u)} S_{H_S, z}(u) du = \frac{\sigma_z(u)}{z(u)} \left[\int_0^1 S_{H_S, z}(u) du \right]. \quad (35)$$

The term in square brackets on the right of Eq. (35) is plotted in Fig. (8).

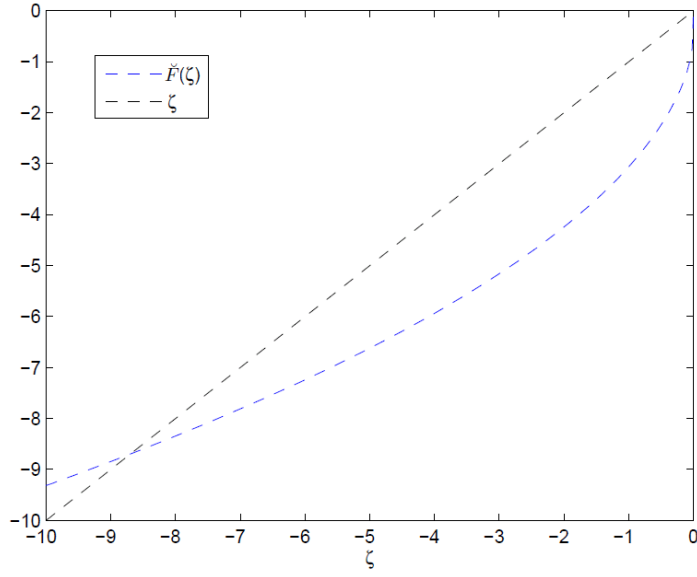


Fig. 5. Graphical visualization of the fixed point solution of Eq. (25). The recursively defined series $[\check{F}(\zeta_{guess}), \check{F}(\check{F}(\zeta_{guess})), \check{F}(\check{F}(\check{F}(\zeta_{guess}))), \dots]$ converges monotonically for any $\zeta_{guess} < 0$. A typical value of $\check{\Lambda} = 3/4$ is used representing unstable conditions in the atmospheric surface layer. The Innavait Creek Basin terrain and beam path are used for $z(u)$, along with the standard path weighting function $G(u)$ as seen in Figs. (3(a)) and (4).

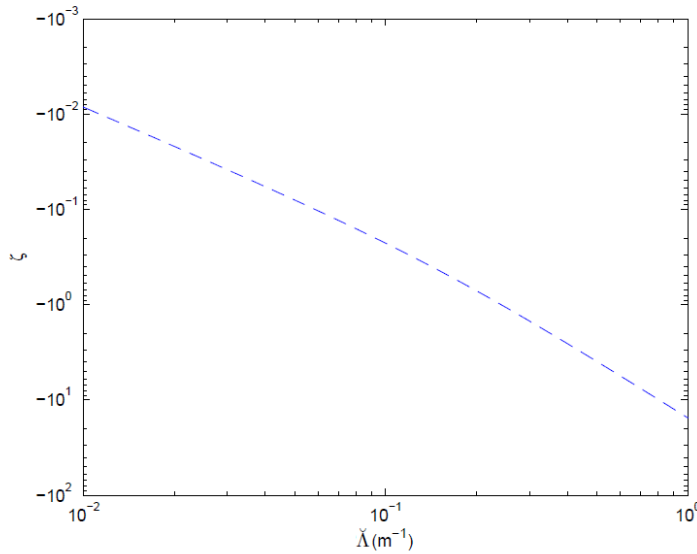


Fig. 6. Solution of Eq. (25) produced with a monotonically converging series as explained in the text and as visualized in Fig. (5). The Innavait Creek Basin terrain and beam path are used for $z(u)$, along with the standard path weighting function $G(u)$ as seen in Figs. (3(a)) and (4). The mapping between ζ and $\check{\Lambda}$ is bijective. Note that the solution of ζ for $\check{\Lambda} = 3/4$ corresponds to the intersection of \check{F} with ζ in Fig. (5).

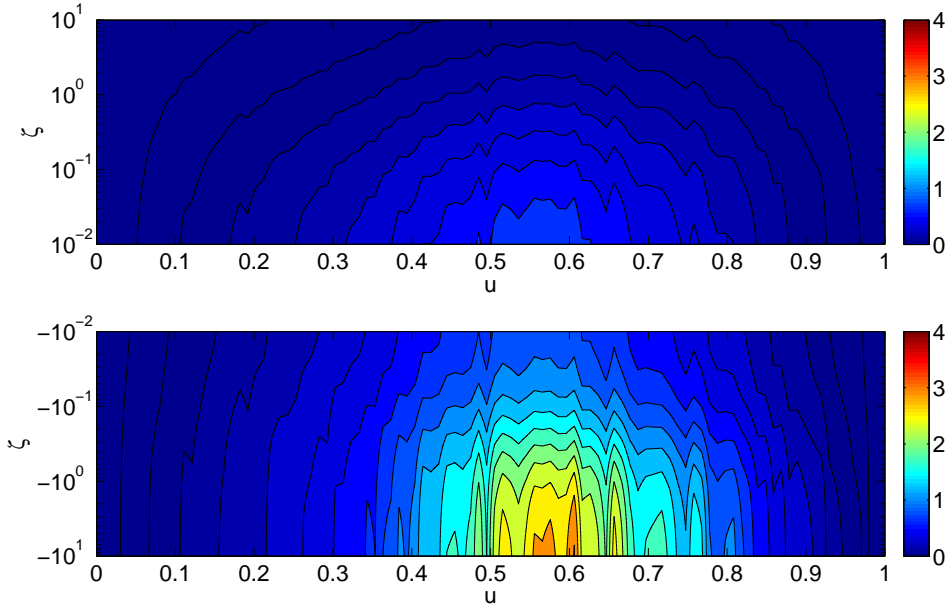


Fig. 7. Sensitivity function $S_{H_S, z}(u) = S_{T_*, z}(u)$. For stable conditions ($\zeta > 0$), $S_{T_*, z}(u)$ is given in Eq. (33). For unstable conditions ($\zeta < 0$), $S_{T_*, z}(u)$ is given by Eq. (34) where values for ζ as a function of $\check{\Lambda}$ are obtained through a numerical solution of Eq. (25) which may be visualized with Fig. (6). The Imnavait Creek Basin terrain and beam path are used for $z(u)$, along with the standard path weighting function $G(u)$ as seen in Figs. (3(a)) and (4).

4.2 Synthetic Scintillometer Beam Paths

It is interesting to examine the sensitivity function over synthetic paths which are representative of commonly used paths in scintillometry. Two synthetic paths can be seen in Fig. (9).

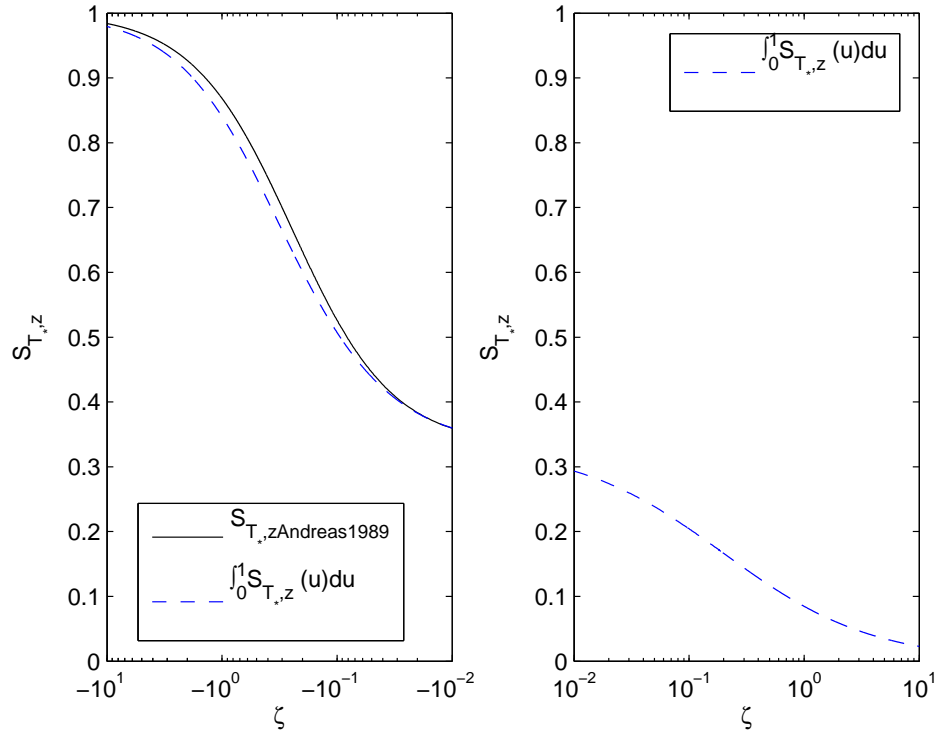


Fig. 8. Average value of $S_{T^*,z}(u) = S_{H_S,z}(u)$ over beam path u , given by $\int_0^1 S_{T^*,z}(u) du$, and the flat terrain sensitivity function S_z derived in Andreas (1989) (for $\zeta > 0$, the functions are identical). For stable conditions ($\zeta > 0$), $S_{T^*,z}(u)$ is given by Eq. (33). For unstable conditions ($\zeta < 0$), $S_{T^*,z}(u)$ is given by Eq. (34) where values for ζ as a function of $\check{\lambda}$ are obtained through a numerical solution of Eq. (25) which may be visualized in Fig. (6). The Innvait Creek Basin terrain and beam path are used for $z(u)$, along with the standard path weighting function $G(u)$ as seen in Figs. (3(a)) and (4).

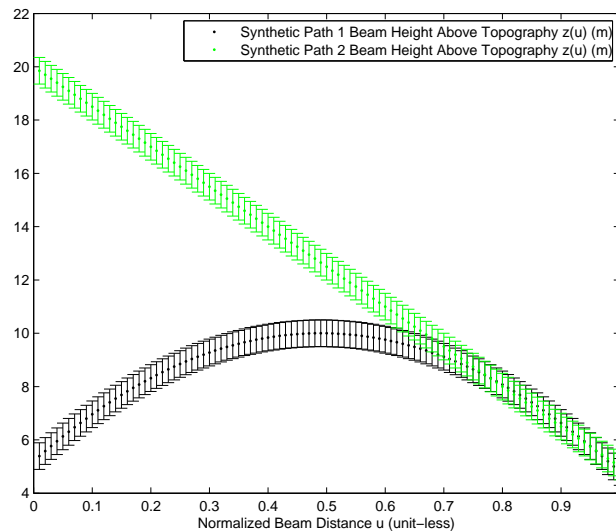


Fig. 9. Synthetic path beam heights.

235 The sensitivity function $S_{T_*,z}(u) = S_{H_S,z}(u)$ for synthetic path 1 seen in Fig. (9) is seen in Fig. (10). For synthetic path 2, the sensitivity function is seen in Fig. (11).

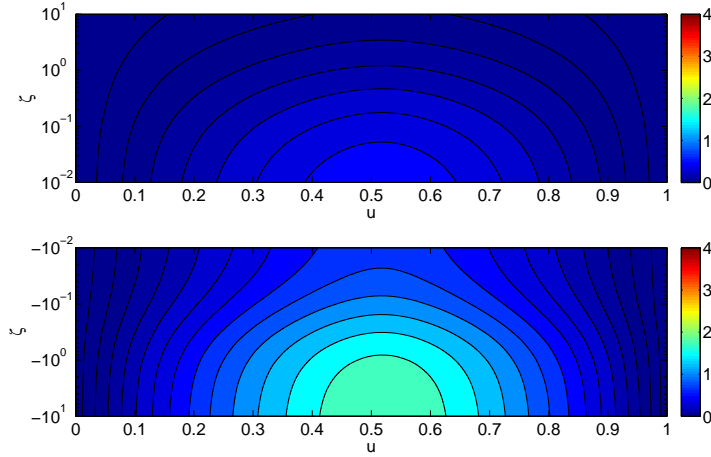


Fig. 10. Sensitivity function $S_{H_S,z}(u) = S_{T_*,z}(u)$. For stable conditions ($\zeta > 0$), $S_{T_*,z}(u)$ is given in Eq. (33). For unstable conditions ($\zeta < 0$), $S_{T_*,z}(u)$ is given by Eq. (34) where values for ζ as a function of $\check{\Lambda}$ are obtained through a numerical solution of Eq. (25) which may be visualized with Fig. (6). Synthetic beam path 1 is used for $z(u)$, along with the standard path weighting function $G(u)$ as seen in Figs. (9) and (4).

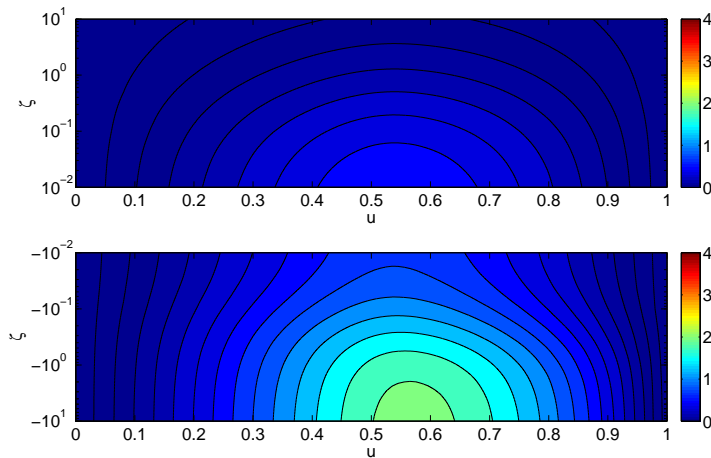


Fig. 11. Sensitivity function $S_{H_S,z}(u) = S_{T_*,z}(u)$. For stable conditions ($\zeta > 0$), $S_{T_*,z}(u)$ is given in Eq. (33). For unstable conditions ($\zeta < 0$), $S_{T_*,z}(u)$ is given by Eq. (34) where values for ζ as a function of $\check{\Lambda}$ are obtained through a numerical solution of Eq. (25) which may be visualized with Fig. (6). Synthetic beam path 2 is used for $z(u)$, along with the standard path weighting function $G(u)$ as seen in Figs. (9) and (4).

5 Discussion

A sensitivity function mapping the propagation of uncertainty from $z(u)$ to H_S has been produced for a large-aperture scintillometer strategy incorporating independent u_* measurements, and the line
 240 integral footprint approach to variable topography developed in Hartogensis et al. (2003) and Kleissl et al. (2008). This was accomplished by mapping out the variable inter-dependency as illustrated in the tree diagrams in Figs. (1) and (2), and by applying the Dirac-Leibniz derivative. The solution to $S_{H_S,z}(u)$ is given in Eqs. (15), (33) and (34).

245 As seen in Figs. (3(a)), (4), and (7), our results for $S_{T_*,z}(u) = S_{H_S,z}(u)$ show that sensitivity to uncertainties in topographic heights is generally higher in unstable conditions, and it is both concentrated in the center of the path and in areas where the underlying topography approaches the beam height. This finding intuitively makes sense for two reasons: firstly scintillometers are more sensitive to C_T^2 at the center of their beam path, and secondly, C_T^2 decreases nonlinearly in height above
 250 the surface and it strengthens with greater instability. For the Imnavait Creek basin path, the value of $S_{H_S,z}(u)$ increases to 3 at small dips in the beam height beyond the halfway point of the path as seen in Fig. (7). Note that the asymmetry along u of $S_{H_S,z}(u)$ corresponds to the asymmetry of the path which is mostly at a higher ($> 6m$) height in the first half, and at a lower height ($\approx 4m$) in the second half as seen in Fig. (4). Also note that concentrations in $S_{H_S,z}(u)$ occur at roughly $u \approx 60\%$ and
 255 $u \approx 65\%$; these correspond directly to topographic protuberances seen in Figs. (3(a)) and (4). Note that the total error on H_S is contributed from the whole range of u along $S_{H_S,z}(u)$, so even though we may have values of up to 3 in the sensitivity functions, our error bars may still be reasonable. The average value of $S_{H_S,z}(u)$ along u is never higher than 1 as seen in Fig. (8). Knowledge of where the concentration in sensitivity is allows us to greatly decrease our uncertainty by taking high
 260 precision topographic measurements in these areas, especially for Arctic beam paths which must be low due to thin boundary layers. Note also that $S_{H_S,z}(u)$ is not analogous to a footprint or to a path weighting function; the scintillometer is still sensitive to C_T^2 along the whole path. $S_{H_S,z}(u)$ should not be interpreted beyond being a measure of how uncertainties in topographic measurements propagate through to the derived sensible heat flux.

265

The average value of $S_{H_S,z}(u)$ over the beam path reduces to identical results to the flat terrain sensitivity function S_z from Andreas (1989) (which would be denoted $S_{T_*,z}$ here) in stable conditions where z_{eff} is de-coupled from ζ , and nearly identical results (depending on the path) in unstable conditions where z_{eff} is coupled to ζ , as seen in Fig. (8). It is unknown as to whether the
 270 addition of equations for path-averaged u_* measurements such as the Businger-Dyer relation seen in Hartogensis et al. (2003) and Solignac et al. (2009) or displaced-beam scintillometer strategies as seen in Andreas (1992) would change these results significantly.

We note that the study of Hartogensis et al. (2003) evaluated a function similar to $S_{H_S,z}$ for flat
 275 terrain with an independent u_* measurement (2003 Eq. (7) is ignored), however at $\zeta \approx 0$ they found
 a sensitivity of 1/2 instead of 1/3 as found in Andreas (1989). The difference in results between
 these two studies is not due to the differences between single and double wavelength strategies. The
 Obukhov length (denoted by L_{MO} in Hartogensis et al. (2003)) is a function of z_{LAS} through 2003
 Eqs. (5) and (6). The addition of chain rule terms to reflect the dependence of l on z in Hartogensis
 280 et al. (2003) Eq. (A2) resolves differences between Hartogensis et al. (2003) Fig. (A1) and Andreas
 (1989) Fig. (4); the flat terrain sensitivity function for $\zeta < 0$ is

$$S_{H_S,z} = S_{T_*,z} = \frac{1-2b\zeta}{3-2b\zeta} \neq \frac{1-2b\zeta}{2-2b\zeta} = \frac{z}{H_S} \left(\frac{\partial H_S}{\partial z} \right)_l, \quad (36)$$

which is given correctly in Andreas (1989).

Eqs. (9), (11), (33), and (34) may be implemented into computer code for routine analysis of
 285 data. It is worth noting that the sign of ζ is an a-priori unknown from the source measurements.
 Thus, for any set of source measurements, we should calculate the set of all derived variables and
 their respective uncertainties assuming both stable and unstable conditions, and if uncertainties in
 the range of ζ overlap with $\zeta = 0$ for either stability regime, we should then consider the combined
 range of errors on the two sets.

290

In the application of Eq. (9), we must recognize computational error σ_{f_c} . Previous studies have
 incorporated a cyclically iterative algorithm which may not converge as seen in Andreas (2012)
 or which may converge to an incorrect solution as illustrated in the section on coupled nonlinear
 equations in Press et al. (1992). We have developed techniques to eliminate this error. For un-
 295 stable cases ($\zeta < 0$) the solution of ζ follows from Eq. (25) which is in fixed point form. The
 solution to Eq. (25) is guaranteed to converge monotonically with the recursively defined series
 $[\check{F}(\zeta_{guess}), \check{F}(\check{F}(\zeta_{guess})), \check{F}(\check{F}(\check{F}(\zeta_{guess}))), \dots]$ as seen in Traub (1964) and in Agarwal et al.
 (2001), and as demonstrated in Fig. (5). We may solve for the stable case ($\zeta > 0$) recursively using
 Eq. (20), where $\hat{F}(\zeta)$ demonstrates convergence properties which are similar to those of $\check{F}(\zeta)$ in Eq.
 300 (25). It was found practical to make $\zeta_{guess} = \pm 1$.

Future expansions of the results presented here should focus on including multiple wavelength
 strategies to evaluate the latent heat flux and H_S , as well as including path-averaged u_* measure-
 ments using l_o and C_n^2 scintillometer strategies as in Andreas (1992) or using a point measurement
 305 of wind speed and the roughness length via the Businger-Dyer relation (e.g., Panofsky and Dutton,
 1984; Solignac et al., 2009). Modification of the analysis for including path averaged u_* measure-
 ments involves the addition of one or two more equations (e.g., Eq. (8) in Solignac et al. (2009), or
 Eqs. (1.2,1.3) in Andreas (1992)) to substitute into Eqs. (18) and (25), as well as the definition of

new tree diagrams to reflect that u_* is now a derived variable. In these cases, either the turbulence
310 inner scale length l_o or a point measurement of wind speed replaces u_* as a source measurement; u_*
is derived through information from the full set of source measurements. Note that if u_* is derived
through source measurements including z , Eq. (1) implies that $S_{H_S,z} = S_{T_*,z} + S_{u_*,z}$. It is worth
investigating whether computational error can still be eliminated in these cases.

315 We have considered here the effective height line integral approach derived in Hartogensis et al.
(2003) and in Kleissl et al. (2008) to take into account variable topography. Even if we assume a
constant flux surface layer, under realistic wind conditions turbulent air is advected in from nearby
topography. For example, in the Imnavait Creek Basin path seen in Fig. (3(a)), if wind comes from
the West, the turbulent air being advected into the beam path is coming from a volume which is
320 higher above the underlying topography than if wind came from the East. Sensitivity studies should
be produced for two-dimensional surface integral methods which take into account the coupling
of wind direction and topography on instrument footprint (e.g., Meijninger et al., 2002; Liu et al.,
2011). Additionally, new theory may be developed for heterogeneous terrain involving complex dis-
tributions of water availability and roughness length such as the terrain in Imnavait Creek Basin.

325

6 Conclusion

Sensitivity of the sensible heat flux measured by scintillometers has been shown to be highly concen-
trated in areas near the center of the beam path and in areas of topographic protrusion. The general
sensitivity functions evaluated here can be applied for error analysis over any field site. Uncertainty
330 can be greatly reduced by focusing precise topographic measurements in areas of protrusion near
the center of the beam path. The magnitude of the uncertainty is such that it may be necessary to
use high precision LIDAR topographic data in order to reduce what is likely the largest contributor
of uncertainty (Geli et al., 2012). Additionally, computational error can be eliminated by following
a computational procedure as outlined here.

335

Perhaps more important than the results derived here for scintillometers, the new methodology
of the Dirac-Leibniz operator for errors on distributed parameters may be used as a general error
analysis technique in other disciplines.

340 Acknowledgements

Matthew Gruber thanks the Geophysical Institute at the University of Alaska Fairbanks for its sup-
port during his Masters degree. We thank Flora Grabowska of the Mather library for her determi-
nation in securing funding for open access fees, Jason Stuckey and Randy Fulweber at ToolikGIS,

Chad Diesinger at Toolik Research Station, and Matt Nolan at the Institute for Northern Engineering
 345 for the digital elevation map of Imnavait, GPS ground truth measurements, and Fig. 3(b).

7 Individual terms not included in main text for calculation of $S_{T_*,z}(u)$ in the stable case
 ($\zeta > 0$)

$$\left(\frac{\delta T_*}{\delta z}(u)\right) = \left(\left(\frac{\partial T_*}{\partial z_{eff}}\right)_\zeta + \left(\frac{\partial T_*}{\partial \zeta}\right)\left(\frac{\partial \zeta}{\partial z_{eff}}\right)\right)\left(\frac{\delta z_{eff}}{\delta z}(u)\right) \quad (37)$$

$$\left(\frac{\partial T_*}{\partial z_{eff}}\right)_\zeta = \frac{1}{3} \frac{T_*}{z_{eff}} \quad (38)$$

$$350 \quad \left(\frac{\partial T_*}{\partial \zeta}\right) = -T_* \frac{c}{3(1+c\zeta^{2/3})\zeta^{1/3}} \quad (39)$$

8 Individual terms not included in main text for calculation of $S_{T_*,z}(u)$ in the unstable case
 ($\zeta < 0$)

$$\left(\frac{\delta T_*}{\delta z}(u)\right) = \left(\left(\frac{\partial T_*}{\partial z_{eff}}\right)\left(\frac{\partial z_{eff}}{\partial \zeta}\right) + \left(\frac{\partial T_*}{\partial \zeta}\right)_{z_{eff}}\right)\left(\frac{\delta \zeta}{\delta z}(u)\right) \quad (40)$$

$$\left(\frac{\partial T_*}{\partial z_{eff}}\right) = \frac{1}{3} \frac{T_*}{z_{eff}} \quad (41)$$

$$355 \quad \left(\frac{\partial T_*}{\partial \zeta}\right)_{z_{eff}} = -T_* \frac{b}{3(1-b\zeta)} \quad (42)$$

References

- Agarwal, R.P., Meehan, M. and O'Regan, D.: Fixed Point Theory and Applications, 1st edition, Cambridge University Press, Cambridge, United Kingdom, 184 pp, 2001.
- Andreas, E.L.: Two-Wavelength Method of Measuring Path-Averaged Turbulent Surface Heat Fluxes, *J. Atmos. Oceanic Technol.*, 6, 280-292, 1989.
- 360 Andreas, E.L.: Uncertainty in a Path Averaged Measurement of the Friction Velocity u_* , *J. Appl. Meteorol.*, 31, 1312-1321, 1992.
- Andreas, E.L.: Two Experiments on Using a Scintillometer to Infer the Surface Fluxes of Momentum and Sensible Heat, *J. Appl. Meteorol.*, doi: 10.1175/JAMC-D-H-0248-1, 2012.
- 365 Claussen, M.: Area-Averaging of Surface Fluxes in a Neutrally Stratified, Horizontally Inhomogeneous Atmospheric Boundary Layer, *Atmos. Environ.*, 24a, 1349-1360, 1990.
- Claussen, M.: Flux Aggregation at Large Scales: On the Limits of Validity of the Concept of Blending Height, *J. Hydrol.*, 166, 371-382, 1995.
- Edwards, H.M.: Galois Theory, 1st edition, Springer-Verlag, New York, United States, 185 pp, 1984.
- 370 Evans, J., and De Bruin, H.A.R.: The Effective Height of a Two-Wavelength Scintillometer System, *Boundary Layer Meteorol.*, 141, 165-177, 2011.
- Foken, T.: 50 Years of the Monin-Obukhov Similarity Theory, *Boundary Layer Meteorol.*, 119, 431-447, 2006.
- Geli, H.M.E., Neale, C.M.U., Watts, D., Osterberg, J., De Bruin, H.A.R., Kohsiek, W., Pack, R.T., and Hipps, L.E.: Scintillometer-Based Estimates of Sensible Heat Flux Using Lidar-Derived Surface Roughness, *J. Hydrometeorol.*, 13, 1317-1331, 2012.
- 375 Gruber, M.A., and Fochesatto, G.J.: A New Sensitivity Analysis and Solution Method for Scintillometer Measurements of Area-Averaged Turbulent Fluxes, *Boundary Layer Meteorol.*, doi: 10.1007/s10546-013-9835-9, 2013.
- Hartogensis, O.K., Watts, C.J., Rodriguez, J.-C., and De Bruin, H.A.R.: Derivation of an Effective Height for Scintillometers: La Poza Experiment in Northwest Mexico, *J. Hydrometeorol.*, 4, 915-928, 2003.
- 380 Hill, R.J., Ochs, G.R., and Wilson, J.J.: Heat and Momentum Using Optical Scintillation, *Boundary Layer Meteorol.*, 58, 391-408, 1992.
- Kleissl, J., Gomez, J., Hong, S.-H., Hendrickx, J.M.H., Rahn, T., and Defoor, W.L.: Large Aperture Scintillometer Intercomparison Study, *Boundary Layer Meteorol.*, 128, 133-150, 2008.
- 385 Liu, S.M., Xu, Z.W., Wang, W.Z., Jia, Z.Z., Zhu, M.J., Bai, J., and Wang, J.M.: A Comparison of Eddy-Covariance and Large Aperture Scintillometer Measurements With Respect to the Energy Balance Closure Problem, *Hydrol. Earth Syst. Sci.*, 15, 1291-1306, 2011.
- Lu, L., Liu, S., Xu, Z., Yang, K., Cai, X., Jia, L., and Wang, J.: The Characteristics and Parameterization of Aerodynamic Roughness Length over Heterogeneous Surfaces, *Adv. Atm. Sci.*, 26, 180-190, 2009.
- 390 Mason, P.F.: The Formation of Areal-ly-Averaged Roughness Lengths, *Quart. J. Roy. Met. Soc.*, 114, 399-420, 1987.
- Meijninger, W.M.L., Green, A.E., Hartogensis, O.K., Kohsiek, W., Hoedjes, J.C.B., Zuurbier, R.M., and De Bruin, H.A.R.: Determination of Area-Averaged Sensible Heat Fluxes With a Large Aperture Scintillometer Over a Heterogeneous Surface - Flevoland Field Experiment, *Boundary Layer Meteorol.*, 105, 37-62, 2002.
- 395 Moene, A.F.: Effects of Water Vapour on the Structure Parameter of the Refractive Index for Near-Infrared

- Radiation, *Boundary Layer Meteorol.*, 107, 635-653, 2003.
- Monin, A.S., and Obukhov, A.M.: Basic Laws of Turbulent Mixing in the Surface Layer of the Atmosphere, *Tr. Akad. Nauk SSSR Geophys. Inst.*, 24(151), 163-187, 1954.
- Obukhov, A.M.: Turbulence in an Atmosphere With a Non-Uniform Temperature, *Boundary Layer Meteorol.*,
 400 2, 7-29, 1971.
- Ochs, G.R., Wang, T.-I.: Finite Aperture Optical Scintillometer for Profiling Wind and C_n^2 , *Appl. Opt.*, 17,
 3774-3778, 1974.
- Panofsky, H.A., and Dutton, J.A.: *Atmospheric Turbulence: Models and Methods for Engineering Applications*,
 J. Wiley, New York, United States, 397 pp, 1984.
- 405 Press, W.H., Teukolsky, S.A., Vetterling, W.T., Flannery, B.P.: *Numerical Recipes in Fortran: The Art of
 Scientific Computing*, 2nd Edition, Cambridge University Press, Cambridge, United Kingdom, 963 pp, 1992.
- Sasiela, R.J.: *Electromagnetic Wave Propagation in Turbulence: Evaluation and Application of Mellin Trans-
 forms*, 1st Edition, Springer-Verlag, New York, United States, 300 pp, 1994.
- Solignac, P.A., Brut, A., Selves, J.-L., Béteille, J.-P., Gastellu-Etchegorry, J.-P., Keravec, P., Béziat, P., and
 410 Ceschia, E.: Uncertainty Analysis of Computational Methods for Deriving Sensible Heat Flux Values From
 Scintillometer Measurements, *Atmos. Meas. Tech.*, 2, 741-753, 2009.
- Sorbjan, Z.: *Structure of the Atmospheric Boundary Layer*, 1st Edition, Prentice-Hall, New Jersey, United
 States, 317 pp, 1989.
- Tatarskii, V.I.: *Wave Propagation in a Turbulent Medium*, McGraw-Hill Book Company, New York, United
 415 States, 285 pp, 1961.
- Taylor, J.R.: *An Introduction to Error Analysis: The study of uncertainties in physical measurements*, 2nd
 edition, University Science Books, California, United States, 327 pp, 1997.
- Traub, J.F.: *Iterative Methods for the Solution of Equations*, Prentice-Hall, New Jersey, United States, 310 pp,
 1964.
- 420 Wesely, M.: The Combined Effect of Temperature and Humidity on the Refractive Index, *J. Appl. Meteorol.*
 15, 43-49, 1976.
- Wieringa, J.: Roughness-Dependent Geographical Interpolation of Surface Wind Speed Averages, *Quart. J.
 Roy. Met. Soc.* 112, 867-889, 1986.
- Wyngaard, J.C., Izumi, Y., and Collins Jr., S.A.: Behavior of the Refractive-Index Structure Parameter Near the
 425 Ground, *J. Opt. Soc. Am.* 61, 1646-1650, 1971.